Comprehensive Darcy-type law for viscoplastic fluids: Rheology and topology

Emad Chaparian*
James Weir Fluid Laboratory, Department of Mechanical & Aerospace Engineering, University of Strathclyde, Glasgow, United Kingdom

(Received 4 July 2026; accepted 20 October 2026; published 16 November 2026)

We extend our recently proposed framework [Chaparian, Phys. Rev. Fluids **10**, 093301 (2025)] for deriving a Darcy-type law governing viscoplastic flows through porous media to incorporate more applied aspects. In particular, the present work considers a more realistic rheological model (i.e., Herschel-Bulkley, describing the shear-thinning nature of practical yield-stress fluids) along with a wider range of porous media topologies. In our earlier work, the problem was addressed by decomposing the full Bingham number spectrum (representing the ratio of the yield stress of the fluid to the characteristic viscous stress) into three main regions: (i) low Bingham numbers (weak yield stress limit) corresponding to Newtonian flow, (ii) high Bingham numbers (strong yield stress limit) representing yield limit/plastic flow, and (iii) intermediate Bingham numbers (transition regime). By deriving theoretical models for the two asymptotic limits of the spectrum and combining them, we obtained a Darcy-type law applicable across the entire range of Bingham numbers. In contrast to our original work, where the weak yield stress limit reduces to a Newtonian flow, here this limit instead follows a power-law asymptote that captures the shear-thinning dominated behavior of Herschel-Bulkley fluids. In the present study, we derive a scaling to address this limit. The framework is further generalized to incorporate a broader spectrum of porous media topologies, enabling a systematic assessment of how pore geometry influences the resulting macroscopic flow law. The proposed framework provides a unified theoretical basis for predicting yield-stress fluid transport through complex porous media and establishes a pathway toward finding macroscopic models applicable to a wide range of natural systems and industrial processes.

DOI: 10.1103/p9jk-q2kp

I. INTRODUCTION

Complex fluid flow through porous media is ubiquitous in many industrial processes [1–3], biomedical applications [4], and geosciences [5,6]. Due to the complex rheological behavior exhibited by many practical fluids [7,8], macroscale models for flows in porous media are typically semiempirical. However, as reviewed in our previous work [9], a few theoretical studies have proposed a more canonical model in which the pressure gradient is expressed as the sum of two terms associated with the characteristic viscous stress and the yield stress [10–14]. These two terms arise naturally from the physical scaling of the problem.

We rather approached this problem from a more theoretical perspective by splitting the entire problem into three main regimes based on the Bingham number (representing the ratio of the yield

*Contact author: emad.chaparian@strath.ac.uk

Published by the American Physical Society under the terms of the Creative Commons Attribution 4.0 International license. Further distribution of this work must maintain attribution to the author(s) and the published article's title, journal citation, and DOI.

stress of the fluid to the characteristic viscous stress): (i) low Bingham number regime corresponding to the Newtonian flow, (ii) high Bingham number regime corresponding to the yield/plastic limit, and (iii) the intermediate Bingham numbers regime. By deriving models for the two asymptotic limits of the spectrum and combining them, we proposed a Darcy-type law applicable to the entire range of Bingham numbers [9]. In particular, we derived a universal scaling for the yield/plastic limit depends solely on the porosity of the porous medium: the nondimensional critical pressure gradient required to initiate the yield-stress fluid flow inside a porous medium is scaled with the ratio of the obstructed space to the void space of the medium [15]. For the low Bingham number limit—Newtonian limit, we critically reviewed the Darcy laws proposed in the literature and identified the model that best represents the Newtonian regime through comparison with our extensive set of numerical simulations [9].

The present study, which is a sequel to our original work [9], extends this framework to include more realistic behaviours of yield-stress fluid flows in porous media. Specifically, we incorporate the shear-thinning rheology of practical yield-stress fluids and also investigate how different porous media topologies influence the macro-scale responses of these systems.

The proposed framework is founded on accurate description of the two asymptotic limits of the Bingham number spectrum. As demonstrated previously in a variety of yield-stress flow problems (e.g., [16–21]), the yield/plastic limit is independent of the viscous behavior of the fluid. Consequently, simple yield-stress fluids exhibit the same critical pressure gradient for flow initiation, irrespective of their viscous behavior. We show this feature both theoretically and computationally in the present study, implying that the scaling established in [15] remains directly applicable in the present work. The other asymptotic limit, however, requires a different treatment. The weak yield stress limit was reduced to a Newtonian flow in our original work where the Bingham model was considered. Here, by adopting the Herschel-Bulkley constitutive equation to account for the shear-thinning behavior, the corresponding asymptotic limit is analogous to power-law fluid flows. We therefore derive a new theoretical model for the low Bingham number regime that captures the dominant shear-thinning behavior.

Shear-thinning fluid flow in porous media has been studied extensively since the last century in the context of enhanced oil recovery, e.g., [22,23]. A nice review of these studies can be found in [24]. More recently, related problems have also been investigated in fibrous media context, e.g., [25]. Here, we tailor a shear-thinning power-law model for the low Bingham number limit based on a bound derived recently by Castañeda [14] using a homogenisation approach.

Having addressed the two asymptotics, we propose our general Darcy-type law by combining these two models. To validate the proposed law, we perform an exhaustive series of direct numerical simulations (DNS) with augmented Lagrangian method coupled with anisotropic adaptive mesh at the pore scale for a wide range of conditions (i.e., various Bingham numbers, shear-thinning indices, porosities, topologies, etc.)

The outline of the paper is as follows. The next section, Sec. II, sets the problem and introduces the generation procedure of random porous media and computational details. Section III revisits the yield/plastic limit, while the power-law limit (i.e., low Bingham number regime) is addressed in Sec. IV. The resulting asymptotic models are combined in Sec. V to derive the general Darcy-type law. Finally, the study is concluded in Sec. VI.

II. PROBLEM SETUP

A. Mathematical formulation

In this study, we consider incompressible 2D Stokes flows. For the rheological behavior of the fluid, the Herschel-Bulkley constitutive equation is used,

$$\begin{aligned} \hat{\boldsymbol{\tau}} &= \left(\hat{K}\|\hat{\dot{\boldsymbol{\gamma}}}\|^{n-1} + \frac{\hat{\tau}_y}{\|\hat{\dot{\boldsymbol{\gamma}}}\|}\right)\hat{\dot{\boldsymbol{\gamma}}} \quad \text{iff } \|\hat{\boldsymbol{\tau}}\| > \hat{\tau}_y \\ \hat{\dot{\boldsymbol{\gamma}}} &= \mathbf{0} \qquad\qquad\qquad\qquad \text{iff } \|\hat{\boldsymbol{\tau}}\| \leqslant \hat{\tau}_y, \end{aligned} \tag{1}$$

in which $\hat{K}$ is the consistency of the fluid and n is the power-law index. In Eq. (1), $\hat{\dot{\boldsymbol{\gamma}}}$ is the rate-of-strain tensor or indeed $\hat{\boldsymbol{\nabla}}\hat{\boldsymbol{u}} + \hat{\boldsymbol{\nabla}}\hat{\boldsymbol{u}}^T$, where $\hat{\boldsymbol{u}} = (\hat{u}, \hat{v})$ is the fluid velocity vector and $\hat{\boldsymbol{\tau}}$ is the deviatoric stress tensor. The von Mises yielding criterion is considered for the fluid with the yield stress $\hat{\tau}_y$, i.e., $\|\cdot\|$ is the second invariant of a tensor or $\|\boldsymbol{\Lambda}\| = \sqrt{(1/2)\boldsymbol{\Lambda} : \boldsymbol{\Lambda}}$ when $\boldsymbol{\Lambda}$ is deviatoric. To make the equations nondimensional, we use the following scalings:

$$(x, y) = \frac{(\hat{x}, \hat{y})}{\hat{\ell}}, \quad \boldsymbol{u} = (u, v) = \frac{(\hat{u}, \hat{v})}{\hat{U}} \quad \text{and} \quad (p, \boldsymbol{\tau}) = \frac{(\hat{p}, \hat{\boldsymbol{\tau}})}{\hat{K}(\hat{U}/\hat{\ell})^n}.$$

Indeed, the velocity vector is scaled with the interstitial mean velocity at the inlet ($\hat{U}$), and both the deviatoric stress tensor and pressure $\hat{p}$ with the characteristic viscous stress. The length scale $\hat{\ell}$ will be fixed later in this section. Therefore, the fluid flow in the void space (i.e., in $\Omega \setminus \bar{X}$) is governed by the Cauchy equation and continuity,

$$\mathbf{0} = -\boldsymbol{\nabla} p + \boldsymbol{\nabla} \cdot \boldsymbol{\tau} \quad \text{and} \quad \boldsymbol{\nabla} \cdot \boldsymbol{u} = 0, \quad \text{in } \Omega \setminus \bar{X}, \tag{2}$$

and the nondimensional form of the constitutive equation (1) reads

$$\begin{aligned} \boldsymbol{\tau} &= \left(\|\dot{\boldsymbol{\gamma}}\|^{n-1} + \frac{B}{\|\dot{\boldsymbol{\gamma}}\|}\right)\dot{\boldsymbol{\gamma}} \quad && \text{iff } \|\boldsymbol{\tau}\| > B \\ \dot{\boldsymbol{\gamma}} &= \mathbf{0} && \text{iff } \|\boldsymbol{\tau}\| \leqslant B, \end{aligned} \quad \text{in } \Omega \setminus \bar{X} \tag{3}$$

where $B = \hat{\tau}_y/[\hat{K}(\hat{U}/\hat{\ell})^n]$ is the ratio of the yield stress of the fluid to the characteristic viscous stress known as the Bingham number.

Since the interstitial mean velocity is used as the velocity scale in this formulation, the nondimensional flow rate is independent of the Bingham number and is simply equal to the interstitial inlet length L_{inl}; see [9,15,20] for more details. Consequently, the macroscale pressure gradient deriving the flow in a medium depends only on two free parameters: the Bingham number and the power-law index. Therefore, in what follows, for brevity, we denote this dependence by two indices $(\Delta P/L)_{(B,n)}$. The macroscale pressure gradient satisfies the energy balance equation:

$$\begin{aligned} \int_{\Omega\setminus\bar{X}} (\boldsymbol{\tau} : \dot{\boldsymbol{\gamma}}) \mathrm{d}A &= \underbrace{\int_{\Omega\setminus\bar{X}} (\mu\dot{\boldsymbol{\gamma}} : \dot{\boldsymbol{\gamma}}) \mathrm{d}A}_{\text{viscous dissipation}} + \underbrace{B\int_{\Omega\setminus\bar{X}} \|\dot{\boldsymbol{\gamma}}\| \mathrm{d}A}_{\text{plastic dissipation}} \\ &= \int_{\Omega\setminus\bar{X}} \|\dot{\boldsymbol{\gamma}}\|^{n+1} \mathrm{d}A + B\int_{\Omega\setminus\bar{X}} \|\dot{\boldsymbol{\gamma}}\| \mathrm{d}A \\ &= a(\boldsymbol{u}, \boldsymbol{u}) + Bj(\boldsymbol{u}) = \left(\frac{\Delta P}{L}\right)_{(B,n)} \int_{\Omega\setminus\bar{X}} u \mathrm{d}A = L(\boldsymbol{u}), \end{aligned} \tag{4}$$

where $a(\boldsymbol{u}, \boldsymbol{u})$ is the viscous dissipation, $Bj(\boldsymbol{u})$ the plastic dissipation, and $L(\boldsymbol{u})$ the work done by the applied macroscale pressure gradient to derive the fluid flux $\int_{\Omega\setminus\bar{X}} u \, \mathrm{d}A$ through the porous medium.

B. Porous media construction

In the present study, the porous media are generated by randomly distributing mono-size obstacles, of either square or circle shapes, occupying the solid region X in a computational domain Ω of size $\text{meas}(\Omega) = L \times L = 50 \times 50$. More details can be found in our previous works in the same context [9,15,20,26]. The solid volume fraction is denoted by $\phi = \text{meas}(X)/\text{meas}(\Omega)$ and, as a result, the porosity of the medium (i.e., the void fraction) is equal to $1 - \phi$. The dimensionless area of each obstacle is fixed as π, which means that the length scale is $\hat{\ell} = \hat{L}_s/\sqrt{\pi}$, where $\hat{L}_s$ is the square edge length in the case of square obstacles and $\hat{\ell}$ is equal to the radius of obstacles in the case of circular obstacles.

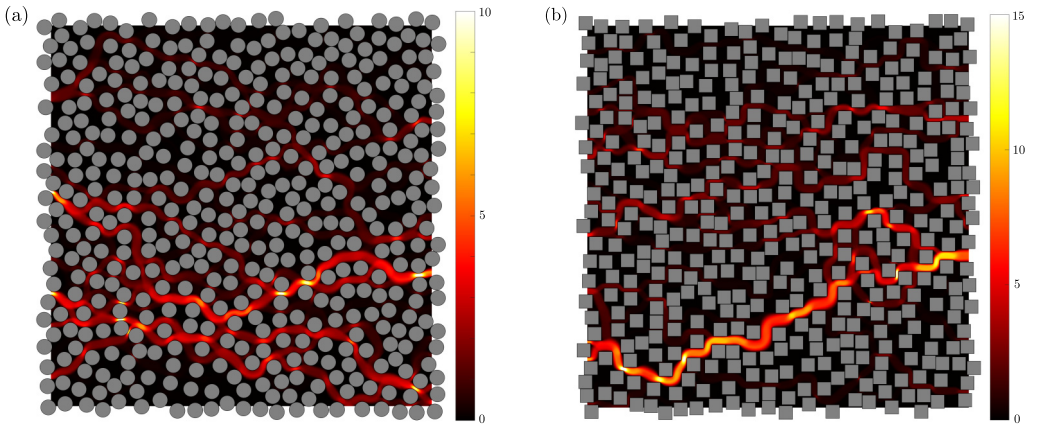


FIG. 1. Contour of velocity $|\boldsymbol{u}|$ for two sample simulations at $\phi = 0.5$. In both panels, $B = 10$ and $n = 0.5$.

C. Methodology

An augmented Lagrangian method [27–29] is implemented in FreeFEM++ (an open-source finite element environment [30]) and is coupled with anisotropic mesh adaptation at the pore scale; see Fig. 3 of [15]. To highlight, the augmented Lagrangian method is capable of handling the nondifferentiable viscoplastic models by relaxing the rate-of-strain tensor. We extensively validated this method for simulating yield-stress fluid flows in various physical settings over past years; see, for example, [16,18,29,31,32]. For the present problem, further details of the numerical implementation, including the boundary conditions and the imposing of the prescribed flow rate, are provided in [9,15,20,26,33]. To illustrate the computational domain and the resulting flow fields, Fig. 1 presents two sample simulations at $B = 10$ and $n = 0.5$ for two different media with $\phi = 0.5$.

III. YIELD/PLASTIC LIMIT: $B \to \infty$

In this section, we revisit the high Bingham number limit which was fully addressed in our recent studies [9,15]. To highlight, in this limit ($B \to \infty$), the energy balance is dominated by plastic dissipation, therefore in the leading order, $Bj(\boldsymbol{u}) \sim L(\boldsymbol{u})$ since the viscous dissipation is at least one order of magnitude smaller. Consequently, Eq. (4) predicts $(\Delta P/L)_\infty \sim B$ since both $j(\boldsymbol{u})$ and flux $\int_{\Omega\setminus\bar{X}} u \, \mathrm{d}A$ reach their asymptotic values in this limit [18]. In other words, the pressure gradient threshold required to initiate flow is therefore independent of the power-law index, which is why only the subscript $_\infty$ is retained in the present notation. This is further confirmed by the computational data presented in Sec. V.

The dependence of $(\Delta P/L)_\infty$ on the topology and porosity of the porous media was addressed in our previous work [15] by developing a model based on the energy equation and the preferred path of the fluid in this limit. The model was then fed with our statiscally sound data generated by pore-network modeling [26], leading to the simple geometrical expression

$$\frac{(\Delta \hat{P}/\hat{L})_\infty}{\hat{\tau}_y/\hat{\ell}} = \pi \frac{\phi}{1-\phi} \Rightarrow \left(\frac{\Delta P}{L}\right)_\infty = \pi \frac{\phi}{1-\phi} B. \tag{5}$$

As demonstrated in [15], although expression (5) is not a direct function of the topology of the medium, it remains highly accurate across a wide range of porous media topologies, including complex random media composed of bi-dispersed polygonal obstacles.

IV. POWER-LAW LIMIT: $B \to 0$

In the present study, the low Bingham number limit differs fundamentally from the Newtonian limit considered in [9] because the fluid is Herschel-Bulkley. Instead, the asymptotic limit $B \to 0$ is analogous to power-law fluid flow. This has been acknowledged both in Al-Fariss and Pinder's model [10] and Castañeda's upper bound calculations [14]. As shown by Castañeda, the upper bound of the macroscale pressure gradient is

$$\left(\frac{\Delta P}{L}\right)_{(B,n)} \leqslant \frac{(1-\phi)^{\frac{1-n}{2}}}{\kappa_{(0,1)}^{\frac{1+n}{2}}} \left(\frac{L_{\text{inl}}}{L}\right)^{n} + \sqrt{\frac{1-\phi}{\kappa_{(0,1)}}}\, B, \tag{6}$$

where $\kappa_{(0,1)}$ is the dimensionless permeability of the medium for a Newtonian fluid (i.e., when $B = 0$ and $n = 1$), which can be written as $(L_{\text{inl}}/L)/(\Delta P/L)_{(0,1)}$. Hence, in the limit of low Bingham numbers ($B \to 0$),

$$\left(\frac{\Delta P}{L}\right)_{(0,n)} \leqslant \left(\frac{\Delta P}{L}\right)_{(0,1)}^{\frac{1+n}{2}} \left(\frac{L_{\text{inl}}/L}{1-\phi}\right)^{\frac{n-1}{2}}, \tag{7}$$

or for a stochastic porous medium ($L_{\text{inl}}/L \equiv 1 - \phi$):

$$\left(\frac{\Delta P}{L}\right)_{(0,n)} \leqslant \left(\frac{\Delta P}{L}\right)_{(0,1)}^{\frac{1+n}{2}}. \tag{8}$$

As mentioned, this is very close to Al-Fariss and Pinder's model, which in the limit of $B \to 0$ predicts

$$\left(\frac{\Delta P}{L}\right)_{(0,n)} = \frac{1}{A(n)} \left(\frac{\Delta P}{L}\right)_{(0,1)}^{\frac{1+n}{2}}, \tag{9}$$

where $A(n) = 4(3 + \frac{1}{n})^{-n}(\frac{3}{50})^{\frac{1-n}{2}}$. Although these two models are derived using fundamentally different theoretical approaches, as discussed in our previous work [9] in detail, they exhibit several common features. Here, in both models, $(\Delta P/L)_{(0,1)}^{(1+n)/2}$ is the scale of the power-law limit pressure gradient; only with a different pre-factor $1/A(n)$.

Figure 2 compares these two expressions with the DNS results spanning three power law indices ($n = 0.25, 0.5$ and 0.75) for eight sample realizations with relatively low and high solid volume fractions ($\phi = 0.1$ and 0.5), and both square and circular obstacle topologies.

As expected, the upper bound (8) is consistently higher than the DNS data with a relatively moderate uncertainty. Expression (9) yields an even larger overprediction of the computed values of $(\Delta P/L)(0, n)$, since the function $A(n)$ is always less than unity for the practically relevant shear-thinning range $n \in [0, 1)$. Nevertheless, Fig. 2 suggests that $(\Delta P/L)_{(0,1)}^{(n+1)/2}$ is a reasonable scaling for the macroscale pressure gradient in the limit $B \to 0$. It should be mentioned that in Fig. 2 (and also later in Fig. 3), the computed Newtonian pressure gradient $(\Delta P/L)_{(0,1)}$ from DNS is substituted in the two expressions (8) and (9).

To further examine this scaling, Fig. 3 presents the computational data for a large set of randomly generated realizations with two solid volume fractions and two types of obstacles, circular and square. Each data point represents the ensemble average of 20 different realizations, with uncertainty bars indicating the minimum and maximum values within the ensemble. As expected, the macroscale pressure gradient decreases with decreasing n due to enhanced shear-thinning behavior. Moreover, for diluter systems (or indeed higher porosities), $(\Delta P/L)_{0,n}$ is lower. More importantly, normalizing the ensemble-averaged pressure gradient by the Newtonian value to the power $(n + 1)/2$, as suggested by expressions (8) and (9), collapses all data into a master curve, irrespective of porosity, obstacle geometry, or power-law index; see Fig. 3(c) and the solid black

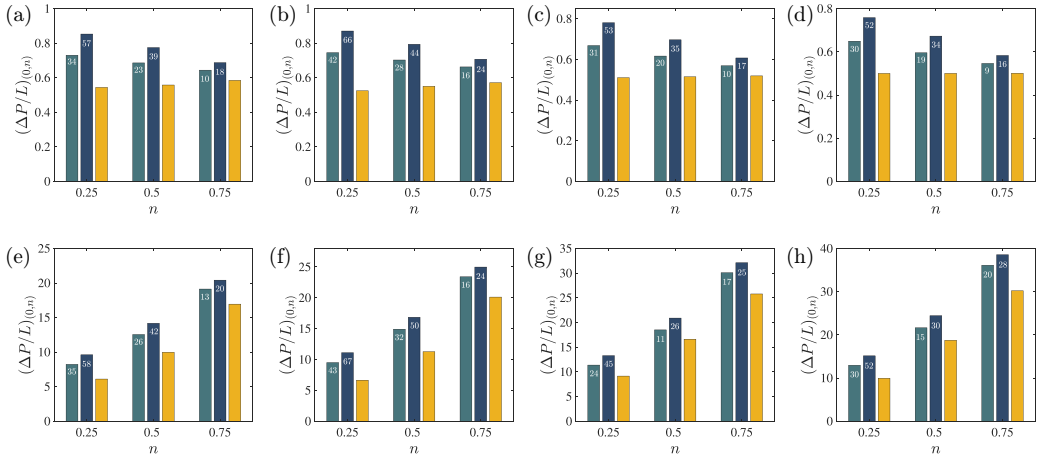


FIG. 2. Comparison of the predicted and computed macroscopic pressure gradients in the power-law limit ($B = 0$) for eight sample realizations for various power law indices ($n = 0.25, 0.5,$ and 0.75). (a)–(d) $\phi = 0.1$; (e)–(h) $\phi = 0.5$. Each panel represents one single realization: (a), (b), (e), (f) circular obstacle cases; (c), (d), (g), (h) square obstacle cases. For each realization, the left bar (green), the middle bar (blue), and the right bar (orange) correspond to the upper bound (8), expression (9), and the DNS result, respectively. The value on each bar indicates the uncertainty/error percentage relative to the DNS result, i.e., the absolute difference between the theoretical prediction and the DNS result, normalized by the DNS value.

line in it. This suggests the following scaling:

$$\frac{(\Delta P/L)_{(0,n)}}{(\Delta P/L)_{(0,1)}^{(n+1)/2}} = g(n) = b\,(n-1) + 1, \tag{10}$$

where $b = 0.4102$ is the fitted value. The function $g(n)$ therefore acts as a correction to the factor $1/A(n)$ in the Al-Fariss and Pinder's model [shown by the dashed line in Fig. 3(c)] and a prefactor for Castañeda's upper bound, thereby closing the gap between the theoretical predictions and the DNS data. This result provides the crucial low Bingham number asymptote required to formulate a general Darcy-type law for Herschel-Bulkley fluid flows through porous media.

V. GENERAL DARCY-TYPE LAW

Having established the asymptotic models for the high Bingham number regime (yield/plastic limit) in Sec. III and the low Bingham number regime (power-law limit) in Sec. IV, we now combine them to construct a general Darcy-type law. Following our framework proposed in [9] for Bingham fluids, the two asymptotic limits are linearly combined, giving

$$\begin{aligned}\left(\frac{\Delta P}{L}\right)_{(B,n)} &= \left(\frac{\Delta P}{L}\right)_{(0,n)} + \left(\frac{\Delta P}{L}\right)_{\infty} \\ &= g(n)\left(\frac{\Delta P}{L}\right)_{(0,1)}^{\frac{1+n}{2}} + \left(\frac{\Delta P}{L}\right)_{\infty} \\ &= [b(n-1)+1]\left(\frac{\Delta P}{L}\right)_{(0,1)}^{\frac{1+n}{2}} + \pi\frac{\phi}{1-\phi}B,\end{aligned} \tag{11}$$

where $(\Delta P/L)_{(0,1)}$ is the dimensionless macroscale pressure gradient for a Newtonian flow through the porous medium. This is the only parameter which has yet to be determined theoretically and is

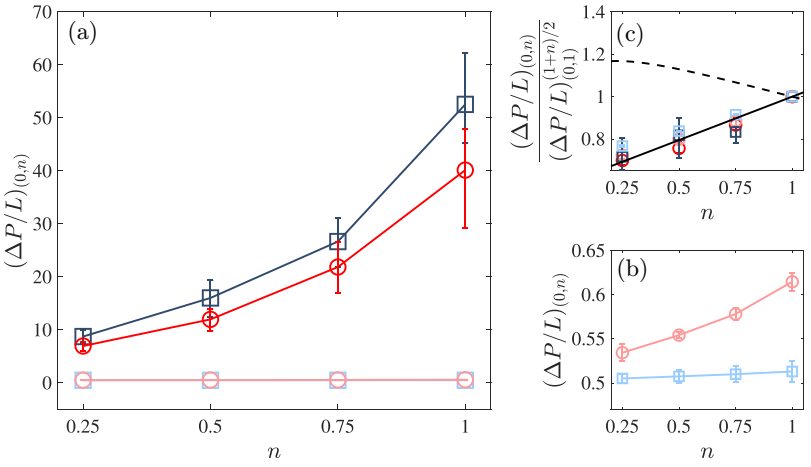


FIG. 3. Ensemble average (20 randomized realizations) of computed macroscale pressure gradient at $B = 0$ for various power-law indices $n = 0.25, 0.5, 0.75,$ and 1. Uncertainty bars indicate the minimum and maximum values within each ensemble. (a) plots $(\Delta P/L)_{(0,n)}$ for circular obstacle cases with red circular symbols and the case of square obstacles with blue square symbols. Dark and light colors correspond to $\phi = 0.5$ and $\phi = 0.1$, respectively. (b) Enlarged view of (a), highlighting the low pressure gradient values associated with $\phi = 0.1$. (c) The scaled pressure gradient: the DNS pressure gradient $(\Delta P/L)_{(0,n)}$ normalized by the scaling proposed in [10,14], i.e., $(\Delta P/L)_{(0,1)}^{(1+n)/2}$. In (c), the dashed black line is $1/A(n)$ while the solid line shows the fitted master curve, $g(n) = b\,(n-1) + 1$, with $b = 0.4102 \pm 0.013$ and RMSE equal to 0.0456.

the sole component of the proposed Darcy-type law (11) through which the topology of the medium enters into the model.

For randomly generated porous media composed of monodispersed square obstacles, we previously adopted a Darcy law which is developed based on the Stokes drag on a 2D object (see [9] for details):

$$\left(\frac{\Delta P}{L}\right)_{(0,1)} = \frac{c}{-\log\phi + d + e\,\phi + f\,\phi^2 + O(\phi^3)}, \tag{12}$$

where $c = 0.4091$, $d = -2.1954$, $e = 4.1141$ and $f = -2.1874$. Figure 4 compares the DNS data for $(\Delta P/L)_{(0,1)}$ obtained for randomly generated porous media composed of mono-dispersed square obstacles (blue solid square symbols) with the above expression (12) (dashed line). To assess the effect of the media topology on the Newtonian macroscale pressure gradient, the corresponding DNS results for porous media composed of monodispersed circular obstacles are also shown for $\phi = 0.1$ and 0.5 (open red circles).

Although both geometries exhibit the same overall trend, a noticeable discrepancy emerges at lower porosities (i.e., case $\phi = 0.5$). Specifically, Newtonian flow through media composed of circular obstacles requires a smaller pressure gradient than the corresponding square obstacle case, consistent with the fact that the drag force on a cylinder is less than the drag force on a 2D object with a square cross section. In contrast, the two geometries' response are nearly identical for the diluter case (i.e., $\phi = 0.1$), indicating that topology becomes important only as the porosity decreases. Nevertheless, the same functional form given by expression (12) could potentially be applied to the circular obstacle cases by refitting the model coefficients against a sufficiently large dataset. Indeed, as discussed in our previous work [9], the functional form of expression (12) was originally proposed for circular obstacles in [34]; see expression (14) of [9].

Here, we instead substitute the Newtonian macroscopic pressure gradient for circular obstacle cases ($\phi = 0.1$ and 0.5) presented in Fig. 4 into our proposed Darcy-type law, i.e., expression (11).

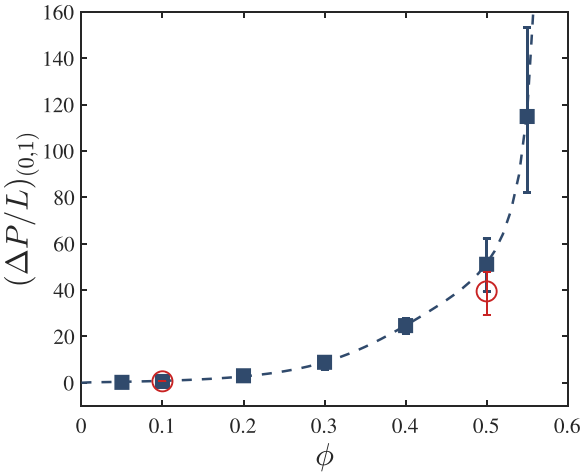


FIG. 4. Dimensionless macroscopic pressure gradient for Newtonian flow ($B = 0$ and $n = 1$) versus solid volume fraction. Solid blue square symbols are ensemble averages of the DNS data obtained from 20 randomized monodispersed square samples at each ϕ, while the open red symbols correspond to the circular obstacle cases. The dashed blue line is expression (12).

The resulting predictions are compared with DNS results in Fig. 5. Red curves represent the model predictions, while blue circular symbols denote ensemble averaged DNS results obtained from 20 independent realizations for each value of ϕ. Dark and light colors correspond to $n = 0.5$ and $n = 1$ (Bingham fluid), respectively. Close agreement can be observed across the entire range of Bingham numbers. The comparison also shows that the influence of shear thinning becomes more pronounced as the solid volume fraction increases. Moreover, in the high Bingham number regime, the computational data for both cases of $n = 0.5$ and $n = 1$ are nearly identical, showing the independence of the critical pressure gradient $(\Delta P/L)_\infty$ from the viscosity behavior of simple yield-stress fluids discussed in Sec. III.

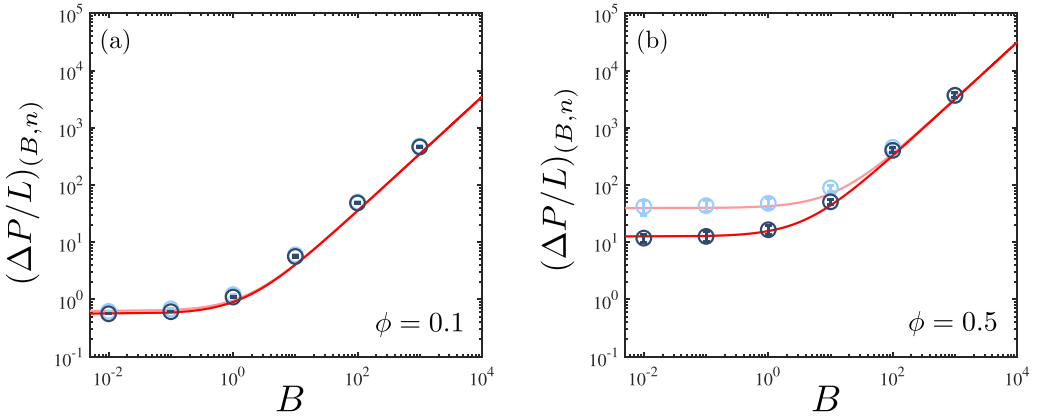


FIG. 5. Macroscale pressure gradient for a Herschel-Bulkley fluid flow through randomized porous media made with circular obstacles: (a) $\phi = 0.1$ and (b) $\phi = 0.5$. Red curves are expression (11), while symbols denote ensemble averaged DNS results with uncertainty bars. Dark and light colors correspond to $n = 0.5$ and $n = 1$, respectively.

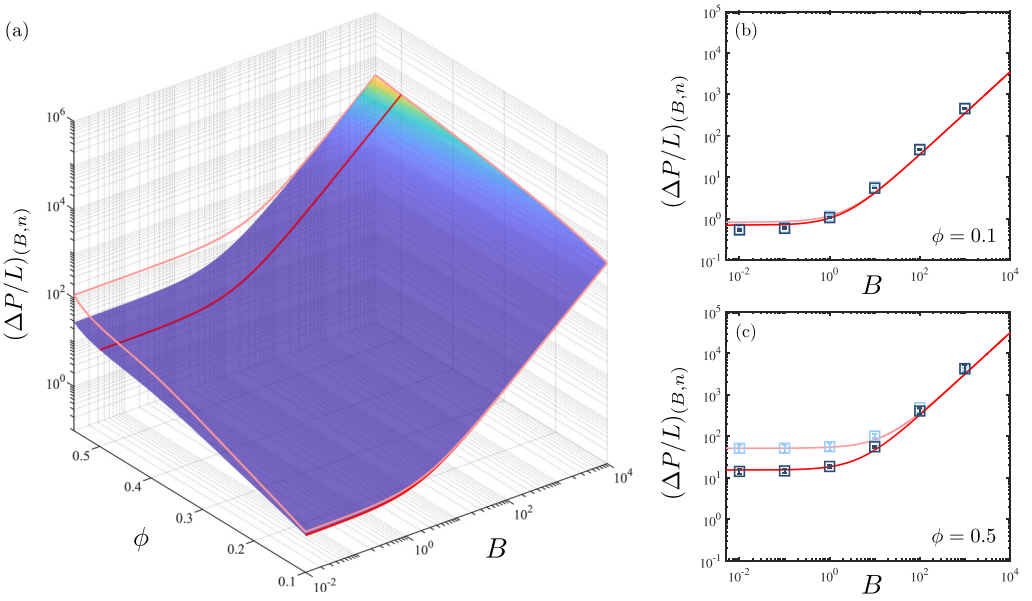


FIG. 6. Macroscale pressure gradient for a Herschel-Bulkley fluid flow through randomized porous media made with square obstacles. The surface in (a) is expression (13) for the case $n = 0.5$ with dark red curves indicating the cross sections at $\phi = 0.1$ and 0.5, which are also shown in (b) and (c) with the same color/style. The light red curves correspond to the Bingham fluid ($n = 1$): in (a) forming the boundary of the surface in the case of a Bingham fluid, and in (b) and (c) representing our proposed Darcy-type law for a Bingham fluid (i.e., expression (30) in [9]). In (b) and (c), symbols represent the ensemble average of the DNS data with uncertainty bars. Dark and light scolors correspond to $n = 0.5$ and $n = 1$, respectively.

Now, to examine the performance of our full Darcy-type law, we substitute $(\Delta P/L)_{(0,1)}$ of the square cases [expression (12)] into the general form (11), yielding

$$\left(\frac{\Delta P}{L}\right)_{(B,n)} = [b\,(n-1)+1]\left(\frac{c}{-\log\phi + d + e\,\phi + f\,\phi^2 + O(\phi^3)}\right)^{\frac{1+n}{2}} + \pi\frac{\phi}{1-\phi}B. \qquad (13)$$

In the case of $n = 1$ (i.e., Bingham fluid), the above expression reduces to our Darcy-law proposed in [9], i.e., expression (30) in the reference. Expression (13) is shown as a surface in Fig. 6(a) for $n = 0.5$. As expected, the pressure gradient increases monotonically with both the Bingham number and the solid volume fraction. The light red color boundary marks the case of a Bingham fluid ($n = 1$), where the limit $B \to 0$ reduces to a Newtonian flow instead. That is why the surface lies below this boundary due to the shear-thinning effects.

The comparison with the DNS data is made in Figs. 6(b) and 6(c) for $\phi = 0.1$ and $\phi = 0.5$ cases, respectively: the proposed law (13) is shown with the dark-red continuous line and the ensemble average DNS data (20 realizations for each ϕ) with dark-blue square symbols. Excellent agreement is observed across the entire range of Bingham numbers, providing strong validity of the proposed Darcy-type law. For reference, the case of a Bingham fluid ($n = 1$) is also shown in Figs. 6(b) and 6(c) using lighter colors.

VI. SUMMARY AND FINAL REMARKS

In this study, we extended our previously proposed Darcy-type law for Bingham fluid flows in porous media [9] to account for both the shear-thinning behavior of yield-stress fluids and the influence of topology of the medium. The objective was to establish a unified macroscopic

relation for the pressure gradient as a function of fluid rheological properties (i.e., B or the Bingham number—the ratio of the yield stress to the characteristic viscous stress—and the power-law index n), together with the porosity $(1-\phi)$ and the topology of the medium:

$$\Delta P/L = f(B, n, \phi, \text{topology}),$$

which is shown by $(\Delta P/L)_{(B,n)}$ in short form for an individual medium where the solid volume fraction and the topology are fixed. For this aim, we followed our original framework proposed for a Bingham fluid and amended the asymptotic models to be able to capture the new effects. Indeed, in our original framework [9], the entire range of Bingham numbers was decomposed into three regimes; two asymptotic low and high Bingham number regimes and an intermediate transition regime with moderate Bingham numbers.

The high Bingham number (yield/plastic) asymptote was retained from our previous work, where the critical pressure gradient (required to initiate the flow due to the yield stress of the fluid) was corroborated to depend only on the porosity of the porous medium; not the exact topology. Therefore, the geometrical scaling for the critical pressure gradient is

$$(\Delta P/L)_{\infty} = \pi \frac{\phi}{1-\phi} B.$$

In addition, as shown in the present study, this asymptote is independent of the viscous behavior of the fluid and therefore remains valid for any simple yield-stress fluid.

The principal extension introduced here concerns the low Bingham number limit. Unlike the Bingham model, for which the weak yield-stress limit reduces to a Newtonian flow, the Herschel-Bulkley fluid approaches a power-law asymptote. Building on earlier theoretical analyses [10,14], together with exhaustive DNS results, we derived the scaling,

$$(\Delta P/L)_{(0,n)} = g(n)\,(\Delta P/L)_{(0,1)}^{(1+n)/2},$$

in which the correction function $g(n) = a(n-1)+1$, found from the master curve fitted to the scaled computed pressure gradients, depends only on the power-law index. In other words, $g(n)$ is independent of both the porosity and the topology of the medium. Consequently, the influence of the medium microstructure/topology enters the proposed framework solely through the Newtonian pressure gradient $(\Delta P/L)_{(0,1)}$, thereby separating the effects of rheology from those of medium geometry. Indeed, two porous media with the same porosities can have different Newtonian permeabilities. This is more pronounced for media with lower porosities.

Combining the two asymptotic models yielded a general Darcy-type law applicable across the entire range of Bingham numbers. Extensive direct numerical simulations demonstrated excellent agreement with our proposed model over a wide range of Bingham numbers, power-law indices, and porosities, providing strong validation of our theoretical framework.

The proposed Darcy-type law establishes a general theoretical framework for predicting yield-stress fluid flows through porous media while clearly separating the respective roles of fluid rheology, porosity of the medium and its microstructure/topology. Extending the present framework to fully three-dimensional and validating it against experimental measurements in our future studies facilitate its application to practical engineering and geophysical systems. Future studies should also broaden the framework to more general porous structures, including anisotropic media.

ACKNOWLEDGMENT

The author acknowledges financial support from Sir David Anderson Bequest Award.

DATA AVAILABILITY

The data that support the findings of this article are not publicly available. The data are available from the authors upon reasonable request.

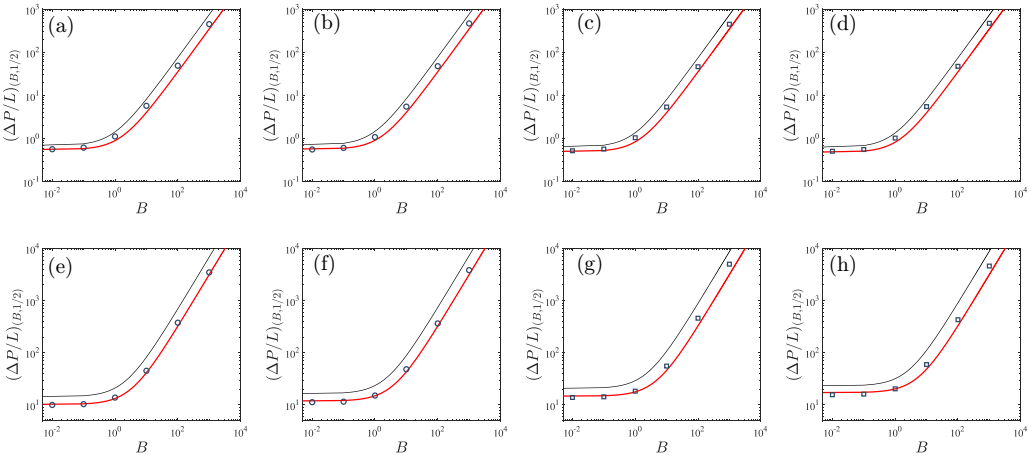


FIG. 7. Comparison of predicted and computed macroscopic pressure gradients for $n = 0.5$ in the eight sample realizations introduced in Fig. 2. (a)–(d) correspond to $\phi = 0.1$ and (e)–(h) to $\phi = 0.5$. Each panel shows a single realization: (a), (b), (e), (f) represent circular obstacle media, and (c), (d), (g), (h) represent square obstacle cases. In all panels, symbols denote DNS results, red lines represent expression (11), and black lines expression (6).

APPENDIX: COMPARISON OF EXPRESSIONS (6) AND (11)

In this Appendix, we compare Castañeda's upper bound, expression (6), and our proposed Darcy-type law (11) with DNS data for the 8 sample realizations introduced in Fig. 2. This is presented in Fig. 7, with each panel corresponding to a single realization: Figures 7(a), 7(b), 7(e), and 7(f) show the circular obstacle cases and Figs. 7(c), 7(d), 7(g), and 7(h) the square obstacle cases. In all panels, symbols denote DNS results, red lines represent our proposed Darcy-type law, and black lines represent Castañeda's upper bound. Note that in all panels, $n = 0.5$. The proposed law agrees closely with the DNS results, and both lie below the upper bound throughout the cases shown.

A more detailed comparison of these two expressions, particularly in the perfectly plastic limit where the proposed Darcy-type law (11) may exhibit some limitations, would be of interest. However, such investigations are beyond the scope of the present study and are left for future work, potentially addressing the uniqueness of solutions in the perfectly plastic limit by analyzing admissible velocity and stress fields.

[1] I. A. Frigaard, K. G. Paso, and P. R. de Souza Mendes, Bingham's model in the oil and gas industry, Rheol. Acta **56**, 259 (2017).

[2] Z. Zhou, H. Zang, S. Wang, X. Du, D. Ma, and J. Zhang, Filtration behaviour of cement-based grout in porous media, Transp. Porous Media **125**, 435 (2018).

[3] A. Skauge, N. Zamani, J. Gausdal Jacobsen, B. S. Shiran, B. Al-Shakry, and T. Skauge, Polymer flow in porous media: Relevance to enhanced oil recovery, Colloids Interfaces **2**, 27 (2018).

[4] J. F. Keating, C. L. Hajducka, and J. Harper, Minimal internal fixation and calcium-phosphate cement in the treatment of fractures of the tibial plateau: A pilot study, J. Bone Joint Surg. Br. **85-B**, 68 (2003).

[5] S. D. C. Walsh and M. O. Saar, Magma yield stress and permeability: Insights from multiphase percolation theory, J. Volcanol. Geotherm. Res. **177**, 1011 (2008).

[6] G. Gustafson and H. Stille, Prediction of groutability from grout properties and hydrogeological data, Tunn. Undergr. Space Tech. **11**, 325 (1996).

[7] D. V. Boger, Rheology of slurries and environmental impacts in the mining industry, Annu. Rev. Chem. Biomol. Eng. **4**, 239 (2013).

[8] P. Coussot, *Rheometry of Pastes, Suspensions, and Granular Materials: Applications in Industry and Environment* (John Wiley & Sons, New York, 2005).
[9] E. Chaparian, Comprehensive Darcy-type law for viscoplastic fluids: Framework, Phys. Rev. Fluids **10**, 093301 (2025).
[10] T. Al-Fariss and K. L. Pinder, Flow through porous media of a shear-thinning liquid with yield stress, Can. J. Chem. Eng. **65**, 391 (1987).
[11] L. Talon and D. Bauer, On the determination of a generalized Darcy equation for yield-stress fluid in porous media using a Lattice-Boltzmann TRT scheme, Eur. Phys. J. E **36**, 139 (2013).
[12] S. Shahsavari and G. H. McKinley, Mobility and pore-scale fluid dynamics of rate-dependent yield-stress fluids flowing through fibrous porous media, J. Non-Newtonian Fluid Mech. **235**, 76 (2016).
[13] D. Bauer, L. Talon, Y. Peysson, H. B. Ly, G. Batôt, T. Chevalier, and M. Fleury, Experimental and numerical determination of Darcy's law for yield stress fluids in porous media, Phys. Rev. Fluids **4**, 063301 (2019).
[14] P. Ponte Castañeda, Variational linear comparison homogenization estimates for the flow of yield stress fluids through porous media, J. Non-Newtonian Fluid Mech. **321**, 105104 (2023).
[15] E. Chaparian, Yielding to percolation: A universal scale, J. Fluid Mech. **980**, A14 (2024).
[16] E. Chaparian and I. A. Frigaard, Yield limit analysis of particle motion in ayield-stress fluid, J. Fluid Mech. **819**, 311 (2017).
[17] I. A. Frigaard, Background lectures on ideal visco-plastic fluid flows, in *Lectures on Visco-Plastic Fluid Mechanics* (Springer, Berlin, 2019), pp. 1–40.
[18] E. Chaparian, D. Izbassarov, F. De Vita, L. Brandt, and O. Tammisola, Yield-stress fluids in porous media: A comparison of viscoplastic and elastoviscoplastic flows, Meccanica **55**, 331 (2020).
[19] J. A. Iglesias, G. Mercier, E. Chaparian, and I. A. Frigaard, Computing the yield limit in three-dimensional flows of a yield stress fluid about a settling particle, J. Non-Newtonian Fluid Mech. **284**, 104374 (2020).
[20] E. Chaparian and O. Tammisola, Sliding flows of yield-stress fluids, J. Fluid Mech. **911**, A17 (2021).
[21] I. A. Frigaard, U = 0? J. Non-Newtonian Fluid Mech. **347**, 105530 (2026).
[22] C. U. Ikoku and H. J. Ramey Jr., Transient flow of non-Newtonian power-law fluids in porous media, Soc. Pet. Eng. J. **19**, 164 (1979).
[23] A. S. Odeh and H. T. Yang, Flow of non-Newtonian power-law fluids through porous media, Soc. Pet. Eng. J. **19**, 155 (1979).
[24] C. B. Shah and Y. C. Yortsos, Aspects of flow of power-law fluids in porous media, AIChE J. **41**, 1099 (1995).
[25] S. Shahsavari and G. H. McKinley, Mobility of power-law and Carreau fluids through fibrous media, Phys. Rev. E **92**, 063012 (2015).
[26] D. Fraggedakis, E. Chaparian, and O. Tammisola, The first open channel for yield-stress fluids in porous media, J. Fluid Mech. **911**, A58 (2021).
[27] N. Roquet and P. Saramito, An adaptive finite element method for Bingham fluid flows around a cylinder, Comput. Methods Appl. Mech. Eng. **192**, 3317 (2003).
[28] R. R. Huilgol and Z. You, Application of the augmented Lagrangian method to steady pipe flows of Bingham, Casson and Herschel–Bulkley fluids, J. Non-Newtonian Fluid Mech. **128**, 126 (2005).
[29] E. Chaparian and O. Tammisola, An adaptive finite element method for elastoviscoplastic fluid flows, J. Non-Newtonian Fluid Mech. **271**, 104148 (2019).
[30] F. Hecht, New development in FreeFEM++, J. Numer. Math. **20**, 251 (2012).
[31] E. Chaparian, C. E. Owens, and G. H. McKinley, Computational rheometry of yielding and viscoplastic flow in vane-and-cup rheometer fixtures, J. Non-Newtonian Fluid Mech. **307**, 104857 (2022).
[32] E. F. Medina-Bañuelos, B. M. Marín-Santibáñez, E. Chaparian, C. E. Owens, G. H. McKinley, and J. Pérez-González, Rheo-PIV of yield-stress fluids in a 3D-printed fractal vane-in-cup geometry, J. Rheol. **67**, 891 (2023).
[33] S. Parvar, E. Chaparian, and O. Tammisola, General hydrodynamic features of elastoviscoplastic fluid flows through randomized porous media, Theor. Comput. Fluid Dyn. **38**, 531 (2024).
[34] J. E. Drummond and M. I. Tahir, Laminar viscous flow through regular arrays of parallel solid cylinders, Int. J. Multiphase Flow **10**, 515 (1984).